Materials Science & Engineering A 822 (2021) 141669

Contents lists available at ScienceDirect

Materials Science & Engineering A

journal homepage: www.elsevier.com/locate/msea

Cyclic deformation and fatigue behavior of 7075-T651 Al alloy with a gradient structure

Zepeng Liu [a], Hongxia Zhang [a], Zhifeng Yan [a], Peter K. Liaw [b], Peng Dong [a,*]

[a] College of Materials Science and Engineering, Taiyuan University of Technology, Taiyuan, 030024, China
[b] Department of Materials Science and Engineering, The University of Tennessee, Knoxville, TN, 37996, USA

ARTICLE INFO

Keywords:
Aluminum alloy
Surface treatment
Cyclic deformation
Fatigue–life evaluation

ABSTRACT

Fully reversed stress-controlled tension–compression fatigue experiments ($R = -1$) were conducted to study the cyclic deformation and fatigue behavior of 7075-T651 aluminum alloys with and without a surface mechanical rolling treatment (SMRT). The strain amplitude, ratcheting effect, and asymmetric behavior of base metal (BM) and SMRT specimens were analyzed. SMRT specimens showed more remarkable ratcheting effects and tension–compression asymmetry under high stresses. Fatigue tests showed that the fatigue strengths of 7075 Al alloys were increased significantly by the SMRT. Both BM and SMRT specimens presented a failure-mode transition from the intrusions and extrusions failure modes to the $Al_{18}Ti_2Mg_3$ constituent phase. The hysteresis loop was utilized to obtain the plastic-strain amplitude. Furthermore, according to the cyclic-deformation behavior combined with the Manson–Coffin law, strain–life evaluation of BM and SMRT specimens under the stress-control is given.

1. Introduction

Metallic materials with gradient structures, in which grain sizes gradually increase from the surface to the inside, were obtained by means of the surface mechanical attrition treatment (SMAT) [1], surface mechanical grinding treatment (SMGT) [2], or surface mechanical rolling treatment (SMRT) [3], which can simultaneously improve the fatigue properties in low-cycle fatigue (LCF) and high-cycle fatigue (HCF) regimes [4,5]. Although ultrafine-grained (UFG) or nanostructured materials prepared by severe plastic deformation (SPD) [6,7] can significantly improve the fatigue performance, enhanced fatigue properties mostly appear under stress-control and low strain amplitude. SMRT introduces a gradient distribution of grains while introducing a larger compressive residual stress and a gradient distribution of microhardness, making it more difficult for cracks to initiate from the surface, thereby improving fatigue resistance. The fatigue strength and fatigue life after SMRT were significantly improved in different alloy systems, such as pure Cu [8], heat-treatable Al alloys [9], martensitic stainless steels [10], Ni-base superalloys [11], and bearing steels [12].

For materials with internal defects, it will show a tendency of fatigue crack initiation from surface to interior with decreasing stress state [13,14]. It is considered that the *S–N* curves of Al alloy present a continuously decreasing shape and the fatigue crack tends to initiate preferentially from the surface. Until 10^8 cycles or even gigacycle fatigue range, internal and external competitions occur, which usually requires the help of ultrasonic fatigue machine [15]. The introduction of the gradient structure of metallic materials by SMRT to improve fatigue performance also intervenes in the competitive relationship between internal and external crack initiation, so that internal fractures appear under high stress and low cycles, which provides convenience for studying the mechanism of internal crack initiation and propagation of aluminum alloys. It is a recognized fact that under the same stress amplitude, the fatigue life of fatigue crack internal initiation is longer than that of external initiation, which is a key factor for SMRT to induce internal crack initiation to improve fatigue life. This phenomenon has been investigated extensively for various materials, for example, Zhang et al. [12] found that enhanced fatigue property on bearing steel was achieved on the gradient nanostructured sample due to the suppressed fatigue crack initiation at the surface, so that the failure mode changed when the stress amplitude was about 1100 MPa. Shiozawa et al. [16] found that the gradient structure introduced by shot-peening changed the stress amplitude and the corresponding cycles of the fatigue crack from the surface to the inside of a high carbon-chromium bearing steel. Our previous fatigue research [9] on friction-stir-welded Al alloy (R =

* Corresponding author.
E-mail address: dongpeng@tyut.edu.cn (P. Dong).

https://doi.org/10.1016/j.msea.2021.141669
Received 10 March 2021; Received in revised form 25 June 2021; Accepted 28 June 2021
Available online 29 June 2021

0.1) showed that when the fatigue life of the as-welded joint reached 10^7 cycles, fatigue cracks still initiated on the surface of the sample. However, after SMRT, internal crack initiation appeared at about 10^6 cycles, and the fatigue life was significantly improved when the crack initiated inside the specimen.

The cyclic-deformation behavior of metallic materials subjected to SMRT has been extensively studied in martensitic stainless steels [10, 17]. Due to the effect of SMRT, the cyclic deformation behavior of martensitic steel has a significant difference, which makes the secondary hardening more obvious at low strain amplitude. This may be related to the deformation-induced martensite transformation in the gradient nanostructured (GNS) layer after fatigue loading. It is a key factor to improve fatigue performance. However, there are few studies on the cyclic-deformation behavior of aluminum alloys with a gradient structure after SMRT.

Although the fatigue failure mechanisms of metallic materials are diverse, their common feature is that the fatigue damage is mainly caused by irreversible plastic deformation [18]. Whether it is the low-cycle fatigue (LCF), high-cycle fatigue (HCF), or even very-high-cycle fatigue (VHCF), as long as the material undergoes fatigue fracture, plastic deformation will be recorded. Wang et al. [19] showed that the evaluated plastic-strain amplitude is basically on the order of magnitude of 10^{-6} in the concerned VHCF regime. When metallic materials are loaded with different stress ratios, the load stress amplitude is consistent, but the fatigue life is significantly different, showing a significant stress-ratio correlation [20]. Fatigue life under different stress ratios is related to the accumulated plastic-strain amplitude, and the accumulation of plastic strain during cyclic deformation is the main cause of fatigue failure. Therefore, the plastic-strain amplitude (ε_{ap}) in the cyclic deformation process is closely related to the cyclic response and fatigue life [21], and is another key dimension of life prediction, so as to study the role of SMRT in strain-life.

The starting material used in the present work is the 7075-T651 Al alloy, which is extensively used in aerospace and aircraft industries due to its high strength to weight ratio, low density, adequate formability and stable applications. In the current work, starting from the cyclic-deformation and fatigue behavior, the corresponding differences in the cyclic response of BM and SMRT specimens are studied, and the reasons for the fatigue strengthening of SMRT under fully-reversed tension–compression fatigue tests are analyzed. Finally, according to the cyclic-deformation behavior combined with the Manson–Coffin law, the strain–life evaluation under the stress-control of BM and SMRT specimens is given.

2. Experimental details

In this study, 7075-T651 commercial aluminum alloy produced by Alcoa Inc. was used as the base metal (BM), with a nominal thickness of 25 mm. Table 1 shows the nominal chemical composition (weight percent, wt.%), and Table 2 presents the main monotonic mechanical properties. The fatigue specimen was prepared in accordance with ASTM Standard 466. The cylindrical fatigue specimen with a total length of 122 mm had a uniform gauge length of 20 mm and a diameter of 8 mm. The detailed geometry of fatigue specimens was shown in Fig. 1a. The gauge section of the specimen was polished up to an average roughness of 0.2 μm for the experiments.

Part of the machined specimens was subjected to the surface mechanical rolling treatment (SMRT), as shown in Fig. 1a. The SMRT process was achieved by pressing a polished WC/Co ball of 14 mm diameter on the specimen surface with a turning velocity (ν_1) of the sample of 150 rev/min and the moving velocity (ν_2) of the ball along the sample axis of 1 mm/min. After the SMRT procedure was repeated 5 times, the total penetration depth (a_p) of the ball into the sample surface was 250 μm, and the a_p was increased by 50 μm each time, while keeping the processing parameters, ν_1 and ν_2 constants. In the SMRT process, cycling oil was used to lubricate and cool the ball and sample. Stereo microscope (OLYMPUS; SZX16) was used to record the changes in surface roughness before and after SMRT, as shown in Fig. 1b–d. Obviously, after SMRT, the roughness was significantly reduced, and the sample showed a near-polished surface effect.

Table 1
Chemical compositions of the 7075-T651 aluminum alloy (wt.%).

Zn	Mg	Cu	Fe	Si	Cr	Mn	Ti
5.70	2.53	1.66	0.26	0.22	0.20	0.18	0.08

Table 2
Monotonic mechanical properties of the 7075-T651 aluminum alloy.

Yield strength, σ_{YS} (MPa)	Tensile strength, σ_{UTS} (MPa)	Elongation, Δ (%)	Young's modulus, E (GPa)	Poisson's ratio, v
506	545	17.3	71.7	0.33

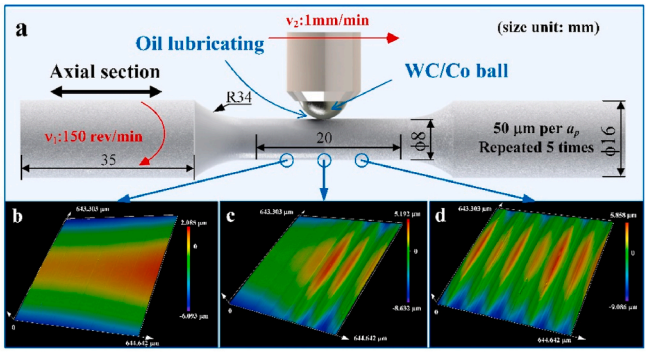

Fig. 1. Schematic of the SMRT (a), and surface roughness comparison before and after SMRT (b–d).

Fully-reversed tension–compression fatigue tests (i.e., stress ratio $R = -1$) were conducted on a SDS100 electro-hydraulic servo-controlled fatigue testing machine at room temperature conducted under a sinusoidal-waveform-stress-controlled mode with a frequency of 1 Hz. During the test, a clip-on extensometer with an axial gauge length of 15 mm attached to the test specimen in the gauge section was used to monitor the real time strain. The stress–strain hysteresis loops were recorded, and each hysteresis loop consisted of 100 data points.

The hardness distribution with depth on the gradient layer was measured with a micro-hardness tester (ZHVST-1000C), equipped with the Vickers indenter. The applied load was 50 g with a holding duration of 15 s. For the SMRT specimens, the micro-hardness is measured from the surface layer to the base material every 10 μm. Along a straight line every 10 μm will cause mutual interference of hardness, so the hardness is measured in the form of a zigzag line.

Microstructural characterization of the SMRT samples was performed, using the electron backscatter diffraction (EBSD; JEOL JSM-7800F) technique. Fractography of the fatigue-fracture samples was analyzed by scanning electron microscopy (SEM; TESCAN MIRA3 LM). Transmission electron microscopy (TEM; JEM-2100F) was used to characterize the microstructure of the gradient layer with an acceleration voltage of 200 kV. The TEM foil was prepared using the focused ion beam (FIB; FEI Helios Nanolab 600i DualBeam System) and lift-out techniques.

3. Results

3.1. Microstructures

Fig. 2 presents the microstructure in EBSD and low-angle grain boundaries (LAGBs) distribution after SMRT. Clearly, a gradient

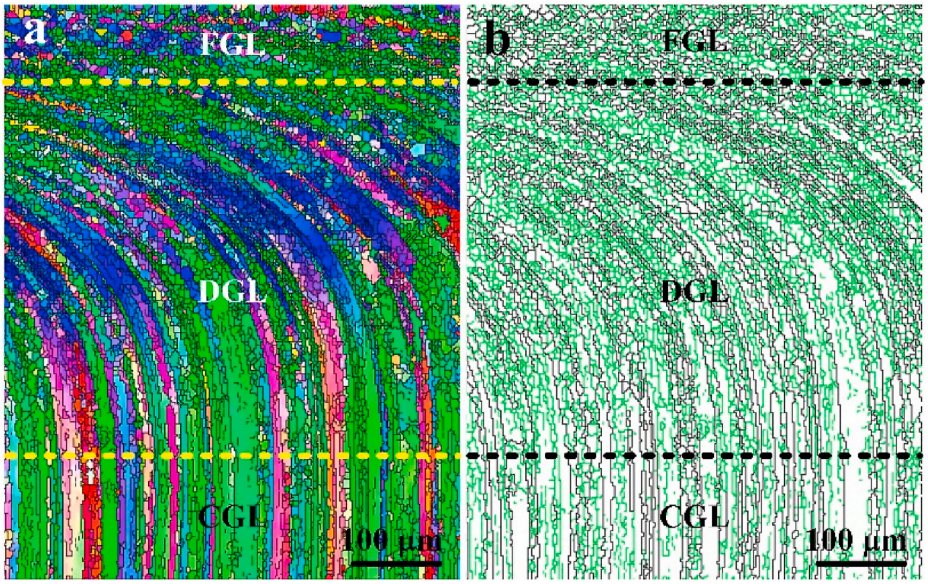

Fig. 2. Gradient layer EBSD image after SMRT (a), and the corresponding LAGBs distribution (b).

structure is formed on the surface of the sample with a thickness of ~500 μm. According to the microstructural characteristics, the SMRT sample can be divided into three zones from the top surface to the inside, namely the surface fine-grain layer (FGL), the deformed-grain layer (DGL), and the coarse-grain layer (CGL). The DGL is characterized by curved grains and a very high density of LAGBs (green lines in Fig. 2b). The BM structure shows the typical rolled structure where grains present elongated characteristics with an average grain width of about 5 μm.

Fig. 3 shows the TEM morphology of the CGL and the corresponding selected area diffraction pattern (SADP). In general, the precipitation sequence of 7XXX series aluminum alloy (AlZnMgCu alloys) can be summarized as follows: supersaturated solid solution (SSSS) → GP zones → η' ($MgZn_2$) → η ($MgZn_2$). The strengthening precipitates in alloy 7075 in the T651 temper are well-established as η′ and the grain-boundary precipitates of η. The purpose of the peak aging state is to achieve the highest strength and hardness. It can be seen from Fig. 3a that a large amount of precipitates are dispersed in the CGL. Comparing with the SADP under the [$\bar{1}$ 1 1] projection with the standard diffraction spots of the η′-phase, η-phase and GP zone of the AlZnMgCu alloy by Stiller et al. [22], it is concluded that the 7075 aluminum alloy base metal is mainly composed of a large amount of η′ precipitates, low density of η precipitates, and GP zones.

In order to further study the microstructure of the gradient layer, FIB technique was used to extract TEM foil near the free surface. The TEM morphology and EBSD image of the FGL layer are shown in Fig. 4. It can be seen from Fig. 4 that the grains of FGL have been significantly refined with the average grain size about 300 nm. Generally, the limit of microstructure refinement is closely related to the grain-boundary structure [23,24]. It is difficult to achieve extreme grain refinement in metals with high-level stacking fault energies, such as Ni, Fe, and Al [25]. Therefore, SMRT performed at room temperature can refine the grains of the aluminum alloy surface layer to several hundred nanometers. Compared with CGL, the number of precipitates of FGL is significantly reduced, and high-density GP zones are distributed inside the refined grains, with an average diameter of less than 5 nm, as shown in Fig. 4c–e.

3.2. Fatigue behavior

Fig. 5 exhibits the fatigue-testing results of the 7075-T651 aluminum alloy of BM and SMRT specimens. The results show that from LCF to HCF regimes, SMRT significantly improves the fatigue strength of aluminum alloy. In the LCF regime, for example, at the cycles of ~10^3, the SMRT specimen fatigue strength is ~6.5% higher than the fatigue strength of the BM specimen. In the HCF regime, the number of cycles exceeds 10^5, the fatigue strength of the SMRT specimen is about 20% greater than that of the BM specimen. Interestingly, the SMRT specimen has a failure mode transition at 290 MPa, while the stress amplitude corresponding to

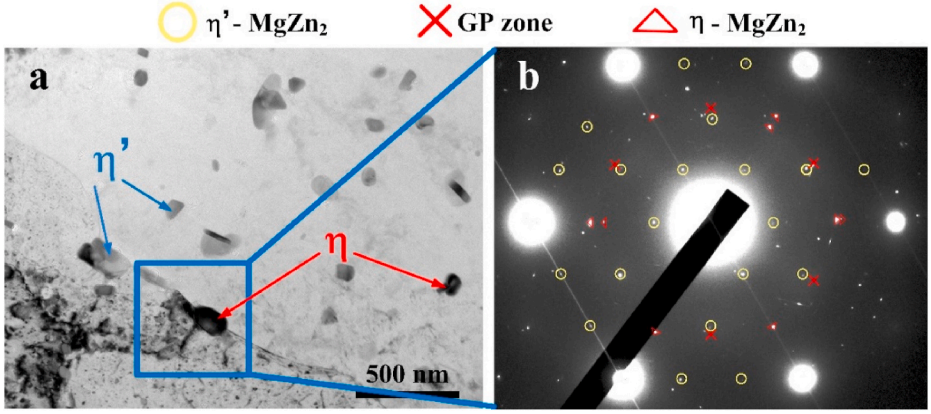

Fig. 3. TEM morphology of CGL (a), and corresponding SADP (b).

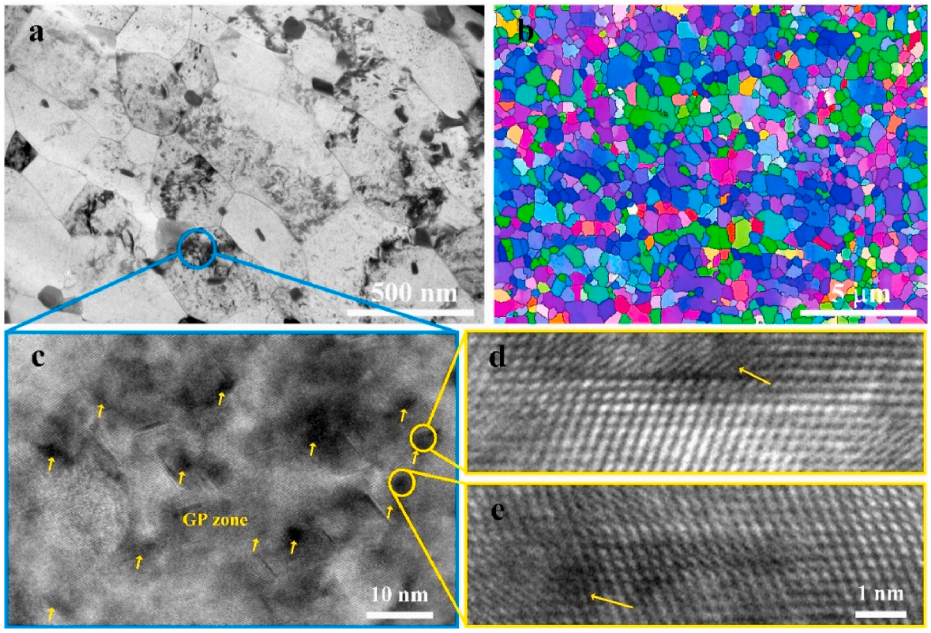

Fig. 4. The TEM morphology of FGL (a), and corresponding EBSD image (b), the GP zones (c) in (a), and the corresponding high-magnification morphology (d–e) of (c).

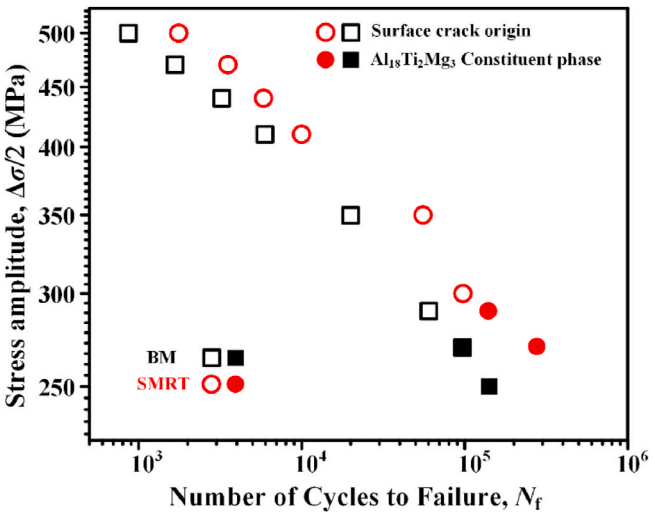

Fig. 5. *S–N* curves of as-received BM and SMRT specimens.

the failure mode transition of the BM specimen is 270 MPa.

Fig. 6 is the SEM image of the BM and SMRT specimens surface-initiation mode under higher stress levels. The fracture morphologies for SMRT and BM specimens failed at $N_f = 1.6 \times 10^3$ and $N_f = 1.95 \times 10^4$, respectively, with the stress amplitude (σ_a) of 410 MPa and 350 MPa, respectively, are plotted in Fig. 6. This surface failure mode can be well-explained by the intrusions and extrusions model.

As the stress level decreases, after the surface-crack initiation, it is clearly seen that the fatigue-crack initiation is located in the interior of SMRT specimens, as shown in Fig. 7. The EDS results show that the crack source is the metal inclusion mainly composed of Al, Ti, and Mg elements, which are consistent with the morphology and size of the cracks that initiated from the internal inclusions when the stress ratio was 0.1. The TEM results [9] showed that the inclusion is an $Al_{18}Ti_2Mg_3$ constituent phase. Since the loading condition of $R = -1$ is more severe than 0.1, existing severe cyclic pressing, so the cycles of the internal fracture occur earlier than $R = 0.1$, about 10^5 cycles. The failure mode of the BM specimen changes at 270 MPa, and the intrusions and extrusions failure mode caused by the slip bands is converted to the $Al_{18}Ti_2Mg_3$ constituent phase to cause fatigue failure, as shown in Fig. 8. The difference of crack initiation from the SMRT specimen is that despite the failure mode transition of the BM specimen, the fatigue cracks are all surface-initiation mode.

3.3. Cyclic deformation behavior

The evolutions of the strain amplitudes during fully-reversed tension–compression fatigue experiments of BM and SMRT specimens are shown in Fig. 9. The horizontal axis is normalized by the cycles under different stress amplitudes when the specimens failure. Furthermore, the strain amplitude is calculated as $(\varepsilon_{max} - \varepsilon_{min})/2$ with ε_{max} and ε_{min} being the maximum tensile and compressive strains of each cycle, respectively. Under different stress amplitudes (as seen in Fig. 9), the strain-amplitude curves can be separated into three stages. Whether it is BM or SMRT, cyclic hardening occurs in the initial stage of cyclic loading, and then the strain amplitude reaches a saturated state. At the end of the fatigue life, unstable cyclic softening eventually leads to material failure. Obviously, the strain amplitude declines as the stress amplitude decreases. In addition, the strain amplitudes corresponding to the half fatigue life under different stresses are extracted for comparison, as presented in Fig. 10. The results show that for a given stress amplitude, the strain amplitudes of BM and SMRT specimens are almost consistent regardless of the high stress or low stress state.

The variation tendency of the mean strains $[(\varepsilon_{max} + \varepsilon_{min})/2]$ of BM and SMRT specimens at half fatigue life is shown in Fig. 10. Both of them show a trend of decreasing first and then increasing with the decline of stress, and the lowest values all appeared around 350 MPa. Table 3 presents the loaded stress amplitude and the corresponding strain amplitude and mean strain for SMRT and BM specimens. It can be seen that even under fully-reversed loading conditions, the ratcheting effect often captured under asymmetric stress loading is also present. The ratcheting strain is also calculated as $\varepsilon_R = (\varepsilon_{max} + \varepsilon_{min})/2$. The change trend of the ratcheting strains of BM and SMRT specimens under different stresses is shown in Fig. 11. Under a high stress ($\sigma_a > 350$ MPa), the ratcheting strain accumulates rapidly in the initial stage, and then the shakedown of ratcheting occurred for cyclic-hardened materials

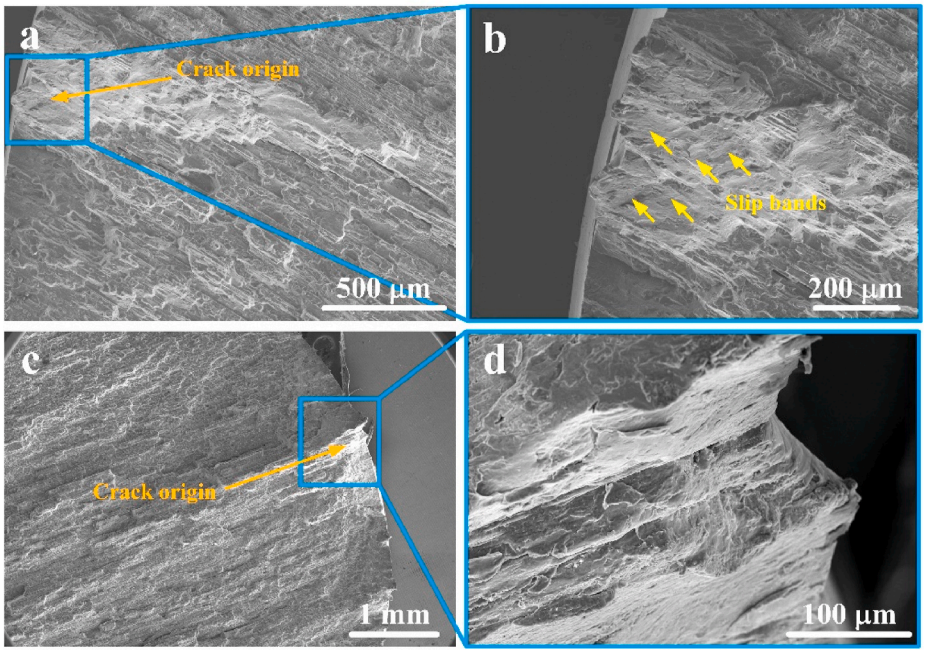

Fig. 6. SEM images of the fracture surface of the SMRT specimen (a–b) under σ_a of 410 MPa and BM specimen (c–d) under σ_a of 350 MPa, both showing the surface-initiation mode.

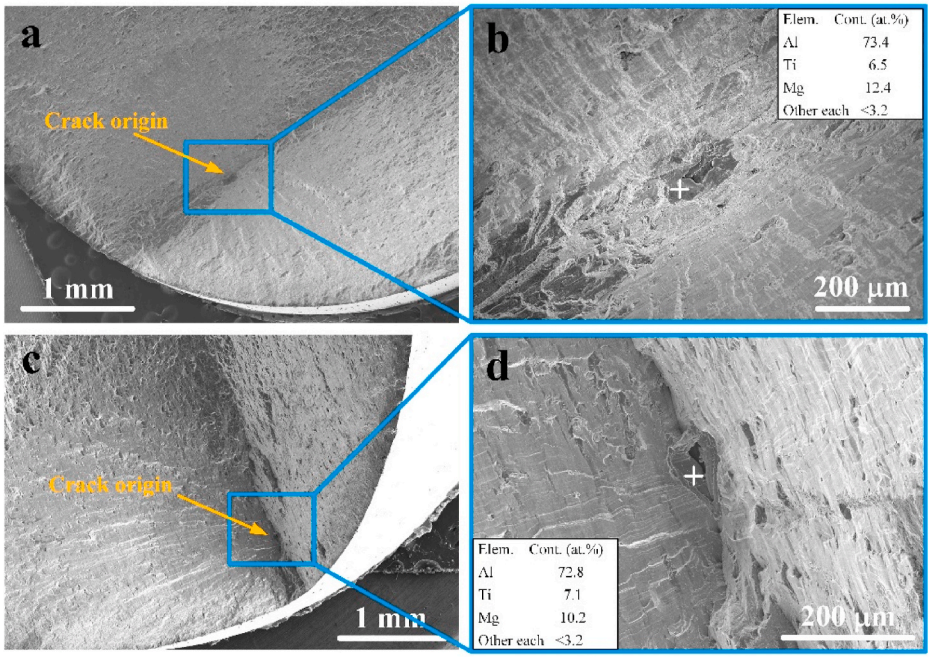

Fig. 7. SEM images of the fracture surface of the SMRT specimens under σ_a of 290 MPa, $N_f = 1.39 \times 10^5$ (a–b), and under σ_a of 270 MPa, $N_f = 2.86 \times 10^5$ (c–d), both showing interior initiation mode.

where almost no ratcheting accumulated after certain cycles. In the final stage, strain instability accumulates and causes material failure. The change trend of the peak tensile strain and the absolute value of the peak compressive strain extracted from the cyclic loading process as a comparison is shown in Fig. 12. In the initial strain-accumulation stage, the tensile strain reaches saturation in a short cycle (about 50 cycles), while the compressive strain value changes greatly, and it takes a long cycle (more than 200 cycles) to reach saturation. Therefore, in the initial stage, the accumulation of ratcheting strain and the appearance of cyclic hardening are more dependent on the compressive strain. Subsequently, both tensile and compressive strains reach saturation. Before failure, the ratcheting strain increases again mainly due to the tensile strain.

When the stress amplitude is 350 MPa, the ratcheting strain is less than zero, and the compressive strain dominates. As the stress continues to decrease, an abnormal law appears. In the initial stage, the mean strain shows a downward trend, such as the BM specimen at 290 MPa and SMRT specimen at 300 MPa. That is to say, this phenomenon is not caused by the introduction of SMRT, which may be attributed to the nonlinear relationship between the peak tensile strain and the deformation resistance of the 7075-T651 aluminum alloy under symmetrical stress.

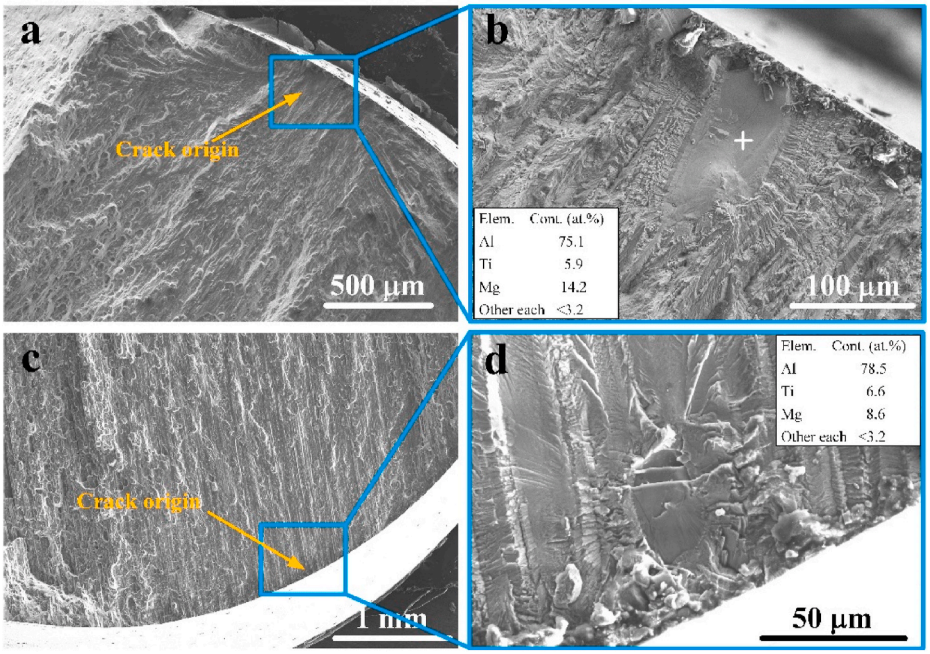

Fig. 8. SEM images of the fracture surface of the BM specimens under σ_a of 270 MPa, $N_f = 9.53 \times 10^4$ (a–b), and under σ_a of 250 MPa, $N_f = 1.43 \times 10^5$ (c–d), both showing surface $Al_{18}Ti_2Mg_3$ constituent phase initiation mode.

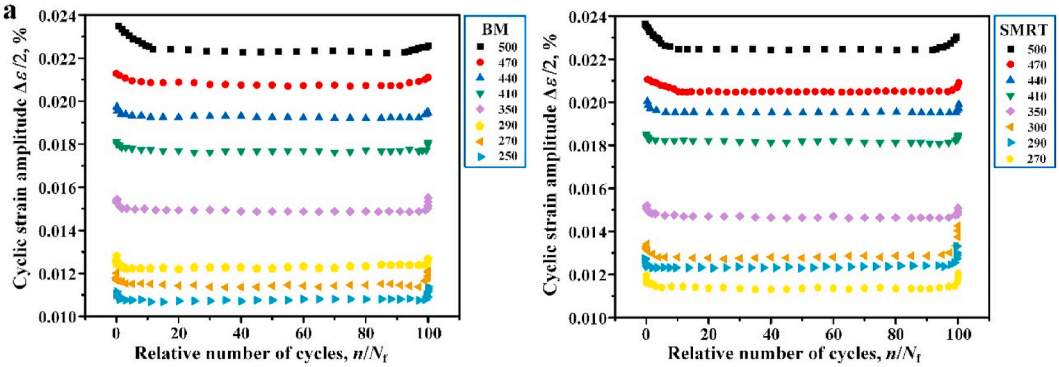

Fig. 9. Strain-amplitudes evolution of BM specimens (a) and SMRT specimens (b) under fully-reversed fatigue tests.

The appearance of this cyclic deformation trend could be caused by changes in the microstructure as stress amplitude decreases. As the stress decreases further, after the abnormal ratcheting strain accumulates, the ratcheting strain law becomes positive again and is consistent with the trend of high stress.

Comparing the ratcheting strain of SMRT and BM specimens (Fig. 10), it can be found that the ratcheting strain of the SMRT specimen is significantly higher than that of BM under a high stress ($\sigma_a > 350$ MPa). However, under a low stress state ($\sigma_a < 350$ MPa), the ratcheting strain of BM and SMRT specimens is not much different. The strain amplitudes of BM and SMRT specimens under the same stress amplitude are keeping consistent, that is to say, the tensile strain of the SMRT specimen is greater than that of BM counterpart, resulting in a more significant ratcheting effect. The ratcheting strain of metal material is a secondary deformation process that increasingly accumulates with the increase of cycles. Therefore, the accumulation of plastic strain along the axial direction and the fatigue accumulated damage are the main causes of accelerated failure of the material [26]. SMRT makes the 7075 Al alloy produce more remarkable ratcheting strain. However, SMRT as an excellent surface-treatment technology can markedly improve the fatigue performance of the material. Therefore, the improvement of the material fatigue performance may be related to the gradient structure generated by SMRT of the aluminum alloy, even if there is a larger ratcheting strain compared with the BM, which will be further discussed in the following sections.

It is worth noting that the failure-mode transition of the BM specimens and the SMRT specimens occurred after the ratcheting strain changed from a negative to positive value and returned to the normal ratcheting strain-accumulation trend. The change trend of the ratcheting strain may be caused by the change of the failure mechanism.

The appearance of the ratcheting strain under the symmetrical stress ratio presents that there is a serious asymmetry in the aluminum alloy during the loading process. Asymmetric behavior under symmetrical stress has been observed in many materials, that is, the resistance to deformation caused by tension and compression is inconsistent, which is a relatively common phenomenon [27], such as the modified 9Cr–1Mo steel [28], single crystals [29], titanium alloys [30], and magnesium alloys [31]. The absolute value difference ($|\varepsilon_{max}| - |\varepsilon_{min}|$) reflects the asymmetric behavior during the fatigue-loading process, and the asymmetric trend of BM and SMRT specimens is shown in Fig. 10. In order to further reveal the asymmetric behavior in the fully-reversed fatigue test, an asymmetry factor, A_σ, proposed by Ma and Wang [29],

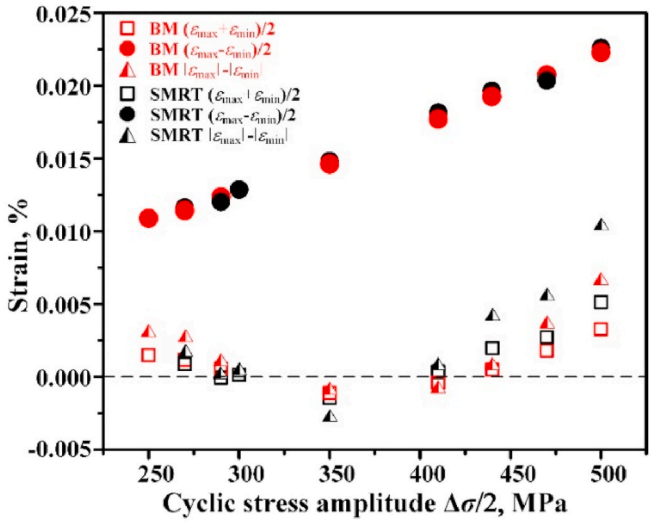

Fig. 10. Evaluation of strain amplitude [($\varepsilon_{max} - \varepsilon_{min}$)/2], mean strain [($\varepsilon_{max} + \varepsilon_{min}$)/2] and absolute strain difference ($|\varepsilon_{max}| - |\varepsilon_{min}|$) at half fatigue life between BM (a) and SMRT specimens (b).

is utilized to evaluate the asymmetry behavior of BM and SMRT specimens under different stresses. A_σ can be calculated as:

$$A_\sigma = \frac{(|\varepsilon_{max}| - |\varepsilon_{min}|)}{(|\varepsilon_{max}| + |\varepsilon_{min}|)/2} \quad (1)$$

where ε_{max} is the tension peak strain, and ε_{min} is the compression peak strain of each cycle, as indicated in Fig. 13. Under a high stress ($\sigma_a > 410$ MPa), both BM and SMRT specimens exist high asymmetry. For example, when $\sigma_a = 500$ MPa, the asymmetry factor of the SMRT specimen reaches 50%, showing severe tension–compression asymmetry behavior. It can be seen that when the stress range is between 500 MPa and 350 MPa, the asymmetry factor of the SMRT specimen is significantly higher than that of the BM specimen, exhibiting more serious asymmetry; when the stress is lower than 350 MPa, the asymmetry factor of the BM specimen is higher than the SMRT specimen. This difference may be attributed to the existence of the gradient layer processed by SMRT.

4. Discussion

4.1. SMRT induced fatigue strengthening

The increase in fatigue strength of the SMRT specimen is mainly due to the generation of a gradient structure, and the grains present a gradient distribution from the surface layer to the matrix. Fig. 14 shows

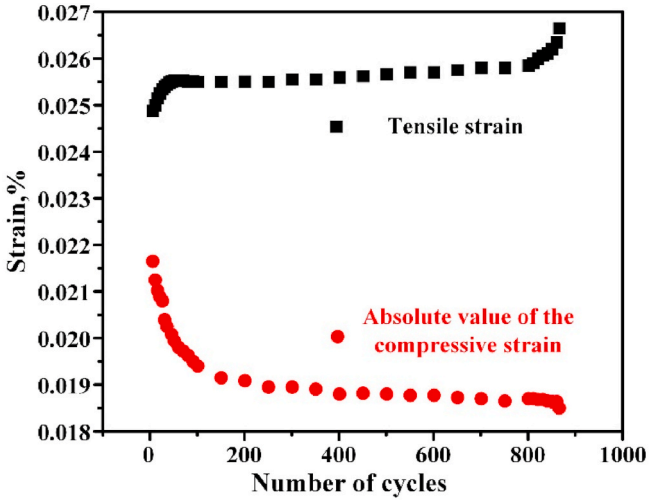

Fig. 12. The change trend of the tensile strain and absolute value of the compressive strain of BM specimen at 500 MPa.

Table 3
Loaded stress amplitude and corresponding strain amplitude and mean strain.

Specimen code (SMRT)	stress amplitude, σ_a (MPa)	strain amplitude, %	mean strain, %	Specimen code (BM)	stress amplitude, σ_a (MPa)	strain amplitude, %	mean strain, %
1	500	2.26×10^{-2}	5.25×10^{-3}	1	500	2.23×10^{-2}	3.28×10^{-3}
2	470	2.04×10^{-2}	2.78×10^{-3}	2	470	2.08×10^{-2}	1.82×10^{-3}
3	440	1.97×10^{-2}	1.58×10^{-3}	3	440	1.93×10^{-2}	5.06×10^{-4}
4	410	1.82×10^{-2}	4.51×10^{-4}	4	410	1.78×10^{-2}	-4.21×10^{-4}
5	350	1.48×10^{-2}	-1.06×10^{-3}	5	350	1.49×10^{-2}	-8.62×10^{-4}
6	300	1.29×10^{-2}	4.86×10^{-4}	6	290	1.24×10^{-2}	5.12×10^{-4}
7	290	1.23×10^{-2}	4.82×10^{-4}	7	270	1.15×10^{-2}	1.37×10^{-3}
8	270	1.12×10^{-2}	7.68×10^{-4}	8	250	1.09×10^{-2}	1.74×10^{-3}

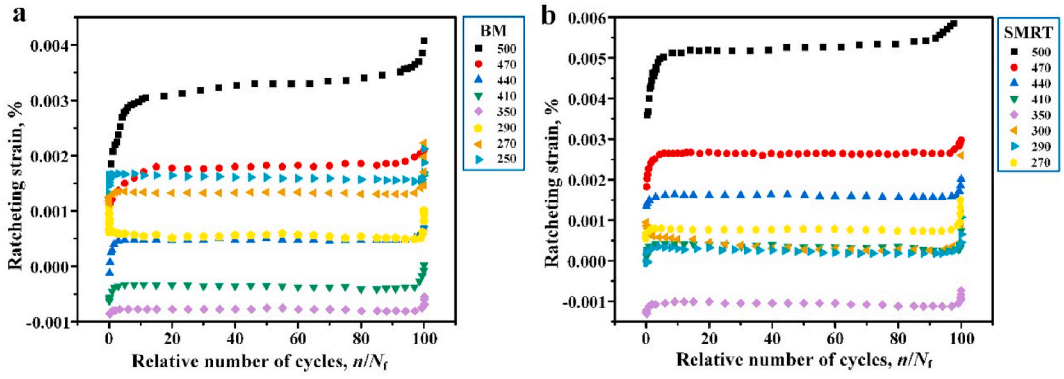

Fig. 11. Ratcheting strain evolution of BM (a) and SMRT (b) specimens under fully-reversed fatigue tests.

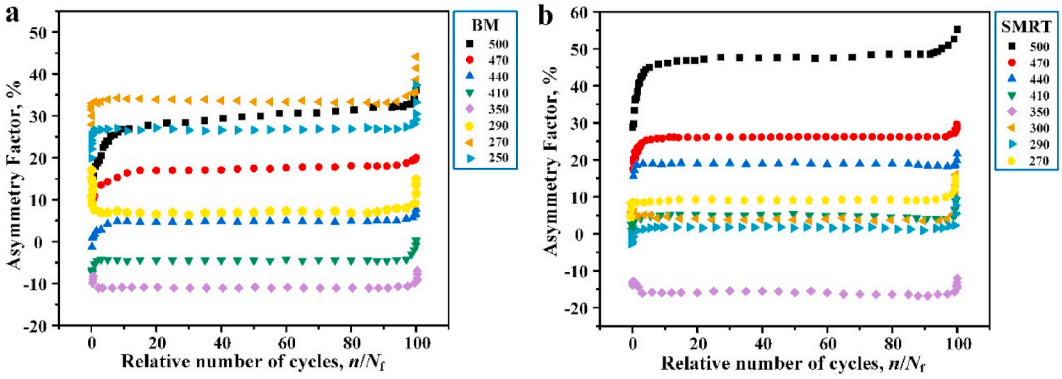

Fig. 13. Evolution of the asymmetry factor for BM (a) and SMRT specimens (b).

the microhardness of the SMRT and BM specimens as a function of depth. The maximum microhardness of the gradient layer appears in the topmost layer of FGL, about 2.6 GPa, and the hardness value gradually decreases with the increase of the distance from the surface layer, and decreases to the matrix value (about 1.8 GPa) at a depth of about 500 μm. In FGL, the grain refinement combined with the strengthening effect of the GP zones (Fig. 4) results in formation of a gradient surface layer with highest microhardness. In DGL, the large plastic deformation produced by SMRT causes severe deformation of the grains, resulting in a high density of LAGBs accompanied by a large number of dislocations, which makes DGL have a higher hardness value. It is well known that refined grains with high strength can effectively inhibit the crack initiation, and coarse grains are beneficial to suppress crack propagation due to their high ductility [32,33]. The coordinated effect of the gradient structure improves the fatigue performance of the specimen. Therefore, the crack nucleation of SMRT specimens is more difficult than that of BM specimens, thus achieving fatigue strengthening under high-stress amplitude (intrusions and extrusions failure mode).

Under high stress amplitudes ($\sigma_a > 350$ MPa), the ratcheting strain of the SMRT specimen was significantly higher than that of the BM counterpart, as shown in Fig. 10, which did not reduce the fatigue strength of the SMRT specimen. The high ratcheting strain produced by the SMRT may be related to the thicker gradient layer on the surface. During cyclic loading, the gradient layer shares part of the tensile strain and suppresses part of the compressive strain [2], making the ratcheting strain remarkable.

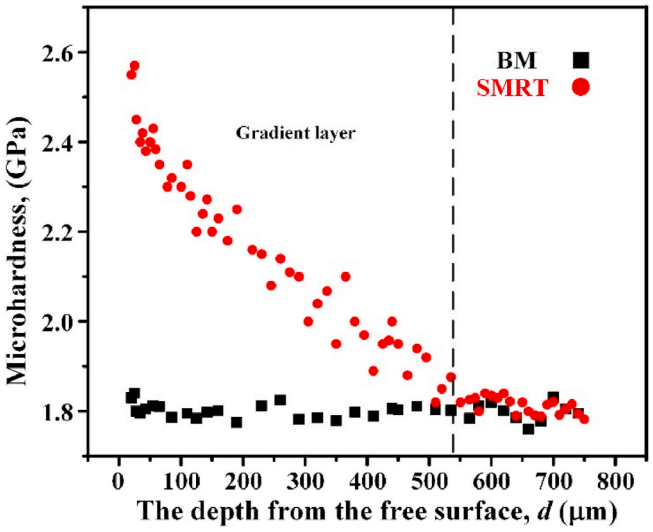

Fig. 14. Variations of microhardness with the distance from a free surface of the SMRT and BM specimens.

With the decrease of stress, the crack sources of BM and SMRT specimens changes, both of which are $Al_{18}Ti_2Mg_3$ constituent phase. When the crack source is $Al_{18}Ti_2Mg_3$ constituent phase, the strengthening effect of the gradient layer on the SMRT specimen inhibits the initiation of fatigue cracks on the surface. This competitive relationship between internal and external crack initiation can be well-explained by stress intensity factor range (ΔK) [15,34,35]. The strengthening effect of SMRT significantly reduces the ΔK at surface defects, reaching a level close to that of the $Al_{18}Ti_2Mg_3$ constituent phase. Due to the effect of large plastic deformation of SMRT, the coarse $Al_{18}Ti_2Mg_3$ phases near the surface are broken, so that cracks preferentially initiate from the inside due to the lack of competition for surface crack initiation. Furthermore, since the BM specimen is a homogeneous material, after reaching the critical stress, the ΔK of the $Al_{18}Ti_2Mg_3$ constituent phase dominates. As fatigue fractures usually initiate at material surfaces and propagate into the interior. Therefore, only the failure-mode transition appears in the BM specimen. Usually the internal fracture is a typical feature of VHCF (fatigue cycles usually greater than 10^7), because the crack-initiation life occupies considerable cycles, which can reach 90% or even more than 99% of the total fatigue life [36]. Simultaneously, It is a recognized fact that under the identical stress level, the fatigue life of fatigue cracks initiating in the interior is longer than in the surface. Consequently, although the crack sources of BM and SMRT specimens are all $Al_{18}Ti_2Mg_3$ phase, since the crack origin of the SMRT specimens initiates in the interior of the specimen, fatigue strengthening under the failure mode of $Al_{18}Ti_2Mg_3$ phase is achieved.

4.2. *Plastic-strain amplitude*

The fatigue loading process is accompanied by significant plastic deformation or microplasticity (order of magnitude of 10^{-6} in the VHCF regime), and the accumulation of plastic strain during cyclic deformation is the main cause of fatigue failure. Therefore, the plastic-strain amplitude (ε_{ap}) in the cyclic deformation process is closely related to the cyclic response and fatigue life. Furthermore, plastic-strain amplitude under different stresses can be obtained by the hysteresis loop, that is, half of the distance between the two intersection points of the hysteresis loop and the horizontal axis is the plastic-strain amplitude. Fig. 15 shows the hysteresis loop of the BM specimen at 250 MPa and the SMRT specimen at 300 MPa. It can be seen from Fig. 15 that from the beginning to the end of loading, the change in the plastic-strain amplitude reflected by the hysteresis loop is not obvious. Therefore, the amplitude corresponding to half of the fatigue life can be used to replace the plastic-strain amplitude under different stresses.

The plastic-strain amplitude obtained through the hysteresis loop can be established with a relationship to the stress amplitude. Their relationship satisfied a power function as follow:

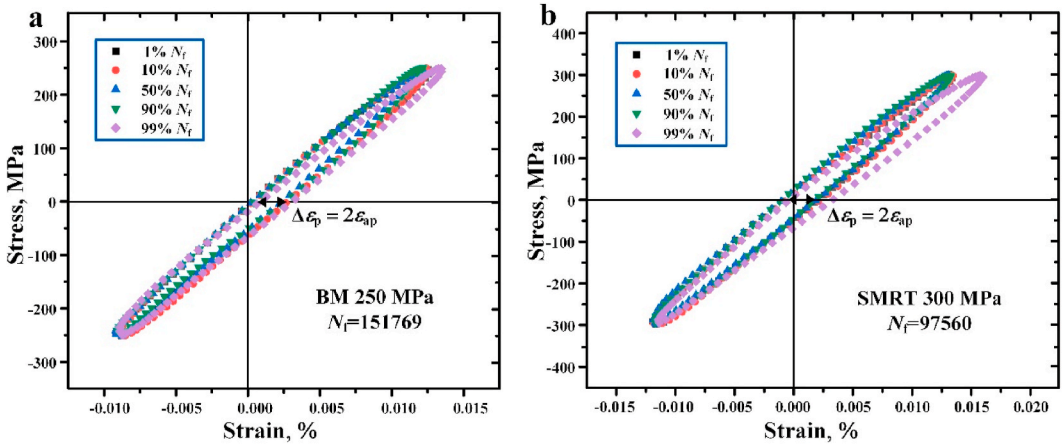

Fig. 15. Hysteresis loops of the BM specimen at 250 MPa (a) and the SMRT specimen at 300 MPa (b).

$$\frac{\Delta\sigma}{2} = k'\left(\frac{\Delta\varepsilon_p}{2}\right)^{n'} \tag{2}$$

where k' represents the cyclic strain hardening coefficient, and n' represents the cyclic strain hardening exponent.

Eq. (2) represents the cyclic stress-strain relationship. The plastic strain amplitude ($\Delta\varepsilon_p/2$) and stress amplitude ($\Delta\sigma/2$) are expressed in double logarithmic coordinates, as presented in Fig. 16. The least square method was used to fit the cyclic stress-strain relationship, showing a good linear correlation. The fitted parameters are listed in Table 4. Obtaining the plastic-strain amplitude through the hysteresis loop provides a method for studying the plastic deformation during the fatigue process for aluminum alloy materials with insignificant cyclic plastic deformation [37].

4.3. Evaluation of fatigue life

For the stress-controlled fatigue test, through the obtained total strain amplitude ($\Delta\varepsilon/2$, from Fig. 9), plastic strain amplitude ($\Delta\varepsilon_p/2$, from Fig. 16) and elastic strain amplitude ($\Delta\varepsilon_e/2$, $\Delta\varepsilon_e/2 = \Delta\varepsilon/2 - \Delta\varepsilon_p/2$), combined with the Manson–Coffin law, the relationship between strain amplitude and fatigue life for BM and SMRT specimens can be fitted, as plotted in Fig. 17. The Manson–Coffin law, formulated as follows:

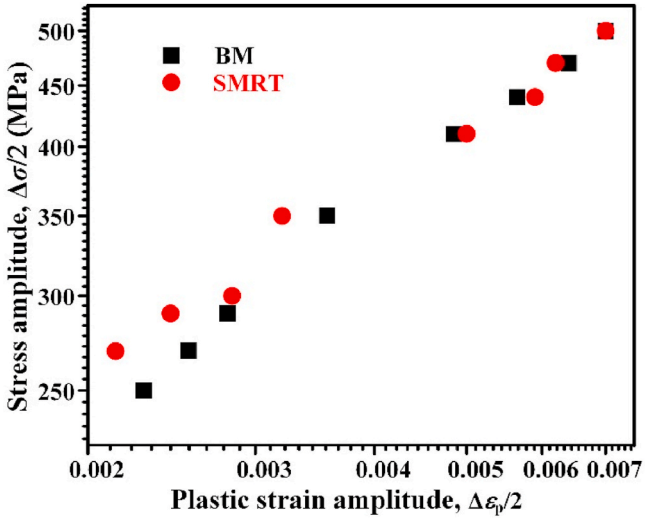

Fig. 16. The stress amplitude of $\Delta\sigma/2$ as a function of plastic strain amplitude of $\Delta\varepsilon_p/2$.

Table 4
Parameters of cyclic strain hardening for BM and SMRT specimens.

	k'	n'
SMRT	6.09×10^3 MPa	0.51
BM	1.05×10^4 MPa	0.61

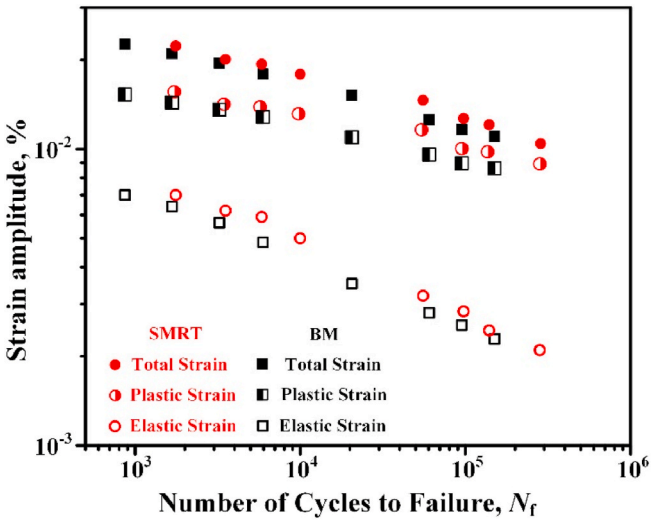

Fig. 17. Strain–life curves of BM and SMRT specimens, containing the relationship between total, elastic and plastic strain and fatigue life.

$$\frac{\Delta\varepsilon}{2} = \frac{\Delta\varepsilon_p}{2} + \frac{\Delta\varepsilon_e}{2} \tag{3}$$

In Eq. (3)

$$\frac{\Delta\varepsilon_p}{2} = \varepsilon_f'(2N_f)^c \tag{4}$$

$$\frac{\Delta\varepsilon_e}{2} = \frac{\sigma_f'}{E}(2N_f)^b \tag{5}$$

where σ_f' represents the fatigue-strength coefficient, b is the Basquin exponent (or fatigue-strength exponent), ε_f' represents the fatigue-ductility coefficient, c is the fatigue-ductility exponent, and E is the elastic modulus. The fitted parameters using the method of least squares applied to the fatigue data for 7075-T651 aluminum alloy are listed in

Table 5
Parameters of Manson–Coffin law for BM and SMRT specimens.

	σ_f'	B	ε_f'	c
SMRT	1.92×10^3 MPa	−0.101	0.054	−0.24
BM	2.03×10^3 MPa	−0.115	0.039	−0.22

Table 5.

The total, elastic, and plastic strain amplitude and the fatigue life present a good linear relationship in the double logarithmic coordinates, as shown in Fig. 17. That is to say, the Manson–Coffin law, typically used for the LCF analysis, is also applied to the HCF regime.

For comparison, the *S–N* curves in Fig. 5 are fitted with the Basquin law (Eq. (6)) using the method of least squares, and the obtained fatigue-strength parameters are shown in Table 6.

$$\frac{\Delta\sigma}{2} = \sigma_f'(2N_f)^b \tag{6}$$

The fatigue-strength parameters fitted by the Basquin law and the Manson–Coffin law are not much different, indicating the reasonability of the strain–life evaluation. It can be seen from Fig. 17 that whether the BM or SMRT specimen, as the stress decreases, the elastic-strain amplitude increasingly approaches the total strain amplitude, that is to say, the plastic-deformation caused by fatigue loading gradually decreases. The SMRT specimen presents higher fatigue ductility than that of BM counterpart in the LCF and HCF regime. Due to the irreversible movement of part of the slip bands under the action of cyclic deformation, it leads to the accumulation of irreversible plastic-deformation and fatigue damage. Whether it is LCF, HCF, or even VHCF regime, as long as the material undergoes fatigue fracture, plastic-deformation will be recorded.

5. Conclusions

Under symmetric tension–compression fatigue tests, cyclic deformation and fatigue behavior of the 7075-T651 Al alloy with and without the surface mechanical rolling treatment were investigated. Some detailed results can be summarized as follows:

(1) Fatigue tests show that the fatigue strength of the 7075 Al alloy is increased significantly by the SMRT within the fatigue life from LCF to HCF regimes. The BM and SMRT specimens have a failure mode transition at 270 MPa and 290 MPa, respectively. Both BM and SMRT specimens, the intrusions and extrusions failure mode caused by the slip bands under a high stress is converted to the $Al_{18}Ti_2Mg_3$ constituent phase under a low stress to cause fatigue failure. The difference with BM specimens is that after the critical point, the fatigue cracks of the SMRT specimens originate inside the specimens, while the BM specimens are all surface-initiation modes. The increase in fatigue strength is mainly related to the strengthening effect of the gradient layer introduced by SMRT.

(2) For a given stress amplitude, the strain amplitudes of BM and SMRT specimens are almost consistent regardless of a high stress or low stress state. The strain-amplitudes curves can be divided into three stages, and cyclic hardening occurs in the initial stage of cyclic loading. The variation tendency of the mean strains of BM and SMRT specimens showed a trend of decreasing first and then increasing with the decline of the stress, and the lowest values all appeared around 350 MPa. The SMRT specimens show a more significant ratcheting effect under a high stress, which may be related to the gradient structure produced by SMRT, which contains considerable low-angle grain boundaries. Furthermore, A_σ is used to evaluate the tension–compression asymmetry behavior under symmetrical loading. Due to the more pronounced ratcheting effect of SMRT under a high stress, it presents more severe asymmetry.

Table 6
Parameters of Basquin law for BM and SMRT specimens.

	σ_f'	B
SMRT	1.62×10^3 MPa	−0.124
BM	1.88×10^3 MPa	−0.142

(3) The hysteresis loop is used to obtain the plastic-strain amplitude. Since the fatigue loading process is accompanied by significant plastic deformation or microplasticity, and the accumulation of plastic strain during cyclic deformation is the main cause of fatigue failure. It is therefore proposed to relate the estimated plastic-strain amplitude with the fatigue lives of the material through the Manson–Coffin law. Moreover, according to the cyclic-deformation behavior combined with the Manson–Coffin law, the strain–life evaluation containing total, plastic, and elastic strain amplitude versus numbers of cycles to failure for BM and SMRT specimens under the stress-control is given.

Data availability

The raw data related to this manuscript will be made available on request.

CRediT authorship contribution statement

Zepeng Liu: Data curation, Formal analysis, Software, Writing – original draft. **Hongxia Zhang:** Funding acquisition, Visualization. **Zhifeng Yan:** Investigation, Validation. **Peter K. Liaw:** Writing – review & editing. **Peng Dong:** Conceptualization, Supervision, Writing – review & editing.

Declaration of competing interest

The authors declare that they have no known competing financial interests or personal relationships that could have appeared to influence the work reported in this paper.

Acknowledgements

The present work was supported by National Natural Science Foundation of China (Grant No. 51505321). P. K. L. very much appreciates the supports from the U.S. National Science Foundation [DMR-1611180 and 1809640] with the program directors, Drs. Judith Yang, Gary Shiflet, and Diana Farkas.

References

[1] W. Chen, Z.S. You, N.R. Tao, Z.H. Jin, L. Lu, Mechanically-induced grain coarsening in gradient nano-grained copper, Acta Mater. 125 (2017) 255–264, https://doi.org/10.1016/j.actamat.2016.12.006.
[2] H.W. Huang, Z.B. Wang, J. Lu, K. Lu, Fatigue behaviors of AISI 316L stainless steel with a gradient nanostructured surface layer, Acta Mater. 87 (2015) 150–160, https://doi.org/10.1016/j.actamat.2014.12.057.
[3] T. Roland, D. Retraint, K. Lu, J. Lu, Fatigue life improvement through surface nanostructuring of stainless steel by means of surface mechanical attrition treatment, Scripta Mater. 54 (2006) 1949–1954, https://doi.org/10.1016/j.scriptamat.2006.01.049.
[4] Y.X. Liu, H. Chen, R.Z. Wang, et al., Fatigue behaviors of 2205 duplex stainless steel with gradient nanostructured surface layer, Int. J. Fatig. 147 (2021) 106170, https://doi.org/10.1016/j.ijfatigue.2021.106170.
[5] T. Hanlon, E.D. Tabachnikova, S. Suresh, Fatigue behavior of nanocrystalline metals and alloys, Int. J. Fatig. 27 (2005) 1147–1158, https://doi.org/10.1016/j.ijfatigue.2005.06.035.
[6] H. Mughrabi, H.W. Höppel, Cyclic deformation and fatigue properties of very fine-grained metals and alloys, Int. J. Fatig. 32 (2010) 1413–1427, https://doi.org/10.1016/j.ijfatigue.2009.10.007.
[7] J.Z. Long, Q.S. Pan, N.R. Tao, M. Dao, S. Suresh, L. Lu, Improved fatigue resistance of gradient nanograined Cu, Acta Mater. 166 (2019) 56–66, https://doi.org/10.1016/j.actamat.2018.12.018.

[8] P. Dong, Z.P. Liu, X. Zhai, Z.F. Yan, W.X. Wang, P.K. Liaw, Incredible improvement in fatigue resistance of friction stir welded 7075-T651 aluminum alloy via surface mechanical rolling treatment, Int. J. Fatig. 124 (2019) 15–25, https://doi.org/10.1016/j.ijfatigue.2019.02.023.
[9] L. Carneiro, X.G. Wang, Y.Y. Jiang, Cyclic deformation and fatigue behavior of 316L stainless steel processed by surface mechanical rolling treatment, Int. J. Fatig. 134 (2020) 105469, https://doi.org/10.1016/j.ijfatigue.2019.105469.
[10] L.L. Shaw, J.W. Tian, A.L. Ortiz, et al., A direct comparison in the fatigue resistance enhanced by surface severe plastic deformation and shot peening in a C-2000 superalloy, Mater. Sci. Eng., A 527 (2010) 986–994, https://doi.org/10.1016/j.msea.2009.10.028.
[11] K. Zhang, Z.B. Wang, K. Lu, Enhanced fatigue property by suppressing surface cracking in a gradient nanostructured bearing steel, Mater. Res. Lett. 5 (2017) 1–9, https://doi.org/10.1080/21663831.2016.1253625.
[12] B. Pyttel, D. Schwerdt, C. Berger, Very high cycle fatigue – is there a fatigue limit? Int. J. Fatig. 33 (2011) 49–58, https://doi.org/10.1016/j.ijfatigue.2010.05.009.
[13] Y.D. Li, L.L. Zhang, Y.H. Fei, X.Y. Liu, M.X. Li, On the formation mechanisms of fine granular area (FGA) on the fracture surface for high strength steels in the VHCF regime, Int. J. Fatig. 82 (2016) 402–410, https://doi.org/10.1016/j.ijfatigue.2015.08.021.
[14] L.P. Xu, Q.Y. Wang, M. Zhou, Micro-crack initiation and propagation in a high strength aluminum alloy during very high cycle fatigue, Mater. Sci. Eng., A 715 (2018) 404–413, https://doi.org/10.1016/j.msea.2018.01.008.
[15] K. Shiozawa, L. Lu, S. Ishihara, S–N curve characteristics and subsurface crack initiation behaviour in ultra-long life fatigue of a high carbon-chromium bearing steel, Fatigue Fract. Eng. M. 24 (2001) 781–790, https://doi.org/10.1046/j.1460-2695.2001.00459.x.
[16] Y.B. Lei, Z.B. Wang, J.L. Xu, K. Lu, Simultaneous enhancement of stress- and strain-controlled fatigue properties in 316L stainless steel with gradient nanostructure, Acta Mater. 168 (2019) 133–142, https://doi.org/10.1016/j.actamat.2019.02.008.
[17] A. Ustrzycka, Z. Mróz, Z.L. Kowalewski, S. Kucharski, Analysis of fatigue crack initiation in cyclic microplasticity regime, Int. J. Fatig. 131 (2020) 105342, https://doi.org/10.1016/j.ijfatigue.2019.105342.
[18] X.G. Wang, E.S. Feng, C. Jiang, A microplasticity evaluation method in very high cycle fatigue, Int. J. Fatig. 94 (2017) 6–15, https://doi.org/10.1016/j.ijfatigue.2016.09.004.
[19] Y.S. Hong, X.L. Liu, Z.Q. Lei, C.Q. Sun, The formation mechanism of characteristic region at crack initiation for very-high-cycle fatigue of high-strength steels, Int. J. Fatig. 89 (2016) 108–118, https://doi.org/10.1016/j.ijfatigue.2015.11.029.
[20] M.C. Marinelli, M. Balbi, U. Krupp, Influence of plastic deformation in fatigue crack behavior in bainitic steel, Int. J. Fatig. 143 (2021) 106014, https://doi.org/10.1016/j.ijfatigue.2020.106014.
[21] K. Stiller, P.J. Warren, V. Hansen, J. Angenete, J. Gjønnes, Investigation of precipitation in an Al–Zn–Mg alloy after two-step ageing treatment at 100° and 150°C, Mater. Sci. Eng., A 270 (1999) 55–63, https://doi.org/10.1016/S0921-5093(99)00231-2.
[22] X.C. Liu, H.W. Zhang, K. Lu, Formation of nano-laminated structure in nickel by means of surface mechanical grinding treatment, Acta Mater. 96 (2015) 24–36, https://doi.org/10.1016/j.actamat.2015.06.014.
[23] K. Lu, Stabilizing nanostructures in metals using grain and twin boundar architectures, Nat. Rev. Mater. 1 (2016) 16019, https://doi.org/10.1038/natrevmats.2016.19.
[24] W. Xu, X.C. Liu, K. Lu, Strain-induced microstructure refinement in pure Al below 100 nm in size, Acta Mater. 152 (2018) 138–147, https://doi.org/10.1016/j.actamat.2018.04.014.
[25] T. Sakai, Y. Sato, N. Oguma, Characteristic S–N properties of high-carbon–chromium-bearing steel under axial loading in long-life fatigue, Fatigue Fract. Eng. M. 25 (2002) 765–773, https://doi.org/10.1046/j.1460-2695.2002.00574.x.
[26] C.B. Lim, K.S. Kim, J.B. Seong, Ratcheting and fatigue behavior of a copper alloy under uniaxial cyclic loading with mean stress, Int. J. Fatig. 31 (2009) 501–507, https://doi.org/10.1016/j.ijfatigue.2008.04.008.
[27] D.L. Wu, P. Zhao, Q.Q. Wang, F.Z. Xuan, Cyclic behavior of 9–12% Cr steel under different control modes in low cycle regime: a comparative study, Int. J. Fatig. 70 (2015) 114–122, https://doi.org/10.1016/j.ijfatigue.2014.08.006.
[28] B.T. Ma, Z.G. Wang, Asymmetry behavior between tension and compression in the cyclic deformation of copper single crystals and other ductile metals, Mater. Sci. Eng., A 129 (1990) 197–206, https://doi.org/10.1016/0921-5093(90)90266-6.
[29] T.K. Heckel, A. Guerrero-Tovar, H.J. Christ, Stress-dependent elastic behavior of a titanium alloy at elevated temperatures, Exp. Mech. 52 (2012) 323–329, https://doi.org/10.1007/s11340-011-9492-1.
[30] Y. Xiong, Q. Yu, Y.Y. Jiang, An experimental study of cyclic plastic deformation of extruded ZK60 magnesium alloy under uniaxial loading at room temperature, Int. J. Plast. 53 (2014) 107–124, https://doi.org/10.1016/j.ijplas.2013.07.008.
[31] H. Mughrabi, H.W. Höppel, M. Kautz, Fatigue and microstructure of ultrafine-grained metals produced by severe plastic deformation, Scripta Mater. 51 (2004) 807–812, https://doi.org/10.1016/j.scriptamat.2004.05.012.
[32] T. Hanlon, Y.N. Kwon, S. Suresh, Grain size effects on the fatigue response of nanocrystalline metals, Scripta Mater. 49 (2003) 675–680, https://doi.org/10.1016/S1359-6462(03)00393-2.
[33] Z.P. Liu, H.X. Zhang, Z.G. Hou, Z.F. Yan, P.K. Liaw, P. Dong, Competitive relationship during fatigue-crack initiation of friction-stir-welded Al alloy, Mater. Sci. Eng., A 809 (2021) 141006, https://doi.org/10.1016/j.msea.2021.141006.
[34] K. Shiozawa, M. Murai, Y. Shimatani, T. Yoshimoto, Transition of fatigue failure mode of Ni–Cr–Mo low-alloy steel in very high cycle regime, Int. J. Fatig. 32 (2010) 541–550, https://doi.org/10.1016/j.ijfatigue.2009.06.011.
[35] Y.S. Hong, Z.Q. Lei, C.Q. Sun, A.G. Zhao, Propensities of crack interior initiation and early growth for very-high-cycle fatigue of high strength steels, Int. J. Fatig. 58 (2014) 144–151, https://doi.org/10.1016/j.ijfatigue.2013.02.023.
[36] S. Sreenivasan, S.K. Mishra, K. Dutta, Ratcheting strain and its effect on low cycle fatigue behavior of Al 7075-T6 alloy, Mater. Sci. Eng., A 698 (2017) 46–53, https://doi.org/10.1016/j.msea.2017.05.048.
[37] N.R. Tao, Z.B. Wang, W.P. Tong, M.L. Sui, J. Lu, K. Lu, An investigation of surface nanocrystallization mechanism in Fe induced by surface mechanical attrition treatment, Acta Mater. 50 (2002) 4603–4616, https://doi.org/10.1016/S1359-6454(02)00310-5.